

Research Network FWF S105

# Photoacoustic Imaging in Medicine and Biology



<http://pai.uibk.ac.at>

---

## **Photoacoustic micro-tomography using optical interferometric detection**

Robert Nuster, Markus Hollota  
Harald Grossauer, Peter Burgholzer  
and Günther Paltauf

September 2009

PAI Report No. 19

---

**FWF**

Der Wissenschaftsfonds.



# Photoacoustic micro-tomography using optical interferometric detection

Robert Nuster<sup>a</sup>, Markus Holotta<sup>b</sup>, Harald Grossauer<sup>c</sup>, Peter Burgholzer<sup>d</sup>, Günther Paltauf<sup>a</sup>

<sup>a</sup>Karl-Franzens-University of Graz, Department of Physics, AUSTRIA

<sup>b</sup>University Hospital of Innsbruck, Department of Radiodiagnostics, AUSTRIA

<sup>c</sup>University of Innsbruck, Department of Mathematics, AUSTRIA

<sup>d</sup>RECENDT Research Center for Non Destructive Testing GmbH, Linz, AUSTRIA

## Abstract

A device for three-dimensional (3D) photoacoustic tomography with resolution in the range of tens of micrometers is presented that uses a light beam for interferometric detection of acoustic waves. Reconstruction of the 3D initial pressure distribution from the signals representing line integrals of the acoustic field is a two-step process. It uses an inversion of two-dimensional wave propagation for obtaining line projections of the initial pressure distribution and the inverse Radon transform. The light beam, propagating freely in a water bath, is scanned either in an arc- or box-shaped curve around the object. Simulations were performed to compare the two scanning procedures. The projection images are obtained either using the filtered back projection algorithm for the  $\pi$ -arc scanning mode or the frequency domain algorithm for the box scanning mode. While the former algorithm provides slightly better image quality the latter is about 20-times faster. The ability of the photoacoustic tomography device to create 3D images with constant resolution throughout the reconstruction volume is demonstrated experimentally using a human hair phantom. These measurements revealed a 3D resolution below 100  $\mu\text{m}$ . In a second experiment, 3D-imaging of an isolated mouse heart is demonstrated to show the applicability for preclinical and biological research.

## 1. Introduction

In various areas of preclinical and biological research, but also in clinical practice there exists a need to obtain three-dimensional (3D) images of small samples (several mm to some cm) with micrometer resolution. Typical targets are whole small animals, isolated organs of small animals or biopsy samples. An established device for this imaging task is the X-ray microtomograph, which was first introduced in the 1980's<sup>1</sup> and has found applications not only in biomedical research but also in other areas such as materials research or electronics. While X-rays give excellent contrast in many kinds of biological samples, alternative contrast mechanisms are often desirable, especially for resolving minute changes of soft tissue composition. In recent years, photoacoustic (PA) (also called optoacoustic) imaging methods have been investigated intensively as a means to reveal structures with optical contrast and a resolution comparable with high frequency ultrasound devices<sup>2-4</sup>. This is achieved by using short light pulses in the nanosecond range to irradiate the investigated object. The diffusely propagating light is absorbed in the object, leading to a small temperature rise and associated thermoelastic pressure. The generated pressure is proportional to the locally deposited energy density, which is in turn given by the local optical absorption coefficient multiplied with the local radiant fluence. In this way the acoustic wave field generated in the sample is strongly influenced by the distribution of tissue chromophores and thus contains important diagnostic information. Measurement of the acoustic field and applying some kind of reconstruction algorithm yields the distribution of initial pressure (right after the light pulse) or energy density<sup>4</sup>. From this distribution also the spatially dependent optical absorption coefficient can be reconstructed<sup>5</sup>, or spectrally dependent values of optical absorption as they are required for quantitative measurements of local blood oxygenation values<sup>6,7</sup>.

High resolution PA imaging has been demonstrated using a microscopy approach with a fixed focus acoustic lens transducer scanning across the surface of an object together with the pulsed illumination beam<sup>8</sup>. Similar resolution for the imaging of superficial blood vessels has

been demonstrated with a point like optical ultrasound sensor scanning over a surface close to an object<sup>9</sup>. Both methods are optimized for the imaging of structures near the surface of an extended object, within a range of several millimeters. They are therefore particularly suited for visualizing blood vasculature in or directly below the skin.

For this kind of half space imaging the detection aperture is always smaller than  $2\pi$ . This aperture is defined as the solid angle occupied by the detection surface, which is the area scanned or covered by detectors, as seen by a point in the imaged object. Exact 3D imaging requires a detection aperture of at least  $2\pi$  for each reconstructed point in the object<sup>10</sup>.

Obviously, this cannot be provided by a limited size, planar arrangement of ultrasound detectors. A curved array or a combination of several planar arrays can yield the desired  $2\pi$  minimum aperture.

In tomographic PA imaging, where a single ultrasound detector scans a curve or surface that encloses the object, the resolution is always limited by the size of the detector. It was shown theoretically that for a circular or spherical scan around an object with a typical commercially available piezoelectric detector having a flat, finite sized active area the resolution is highest in the center of rotation and becomes worse at positions approaching the detection curve<sup>11</sup>.

Increasing the object-detector distance would provide approximately constant resolution throughout the object but at the same time the frequency-dependent damping would tend to decrease high frequency components and therefore deteriorate resolution again. A solution is the use of point like detectors. In particular optical detection can provide at the same time high resolution and sensitivity<sup>3</sup>. Piezoelectric detectors, on the other hand, exhibit decreasing sensitivity with decreasing size.

The method proposed in this work combines small sized detectors and the ability to measure signals from a sufficiently large aperture around an object. It is based on the use of a focused laser beam propagating freely in a coupling liquid surrounding the object as an acoustic detector (Fig. 1). Minute changes of optical phase are integrated along the beam path when it

is crossed by an acoustic wave and are detected interferometrically<sup>12</sup>. A free laser beam as acoustic detector is completely transparent, both optically and acoustically. It can therefore neither disturb the incoming light pulse nor the outgoing acoustic wave. Furthermore, the resolution can be changed by varying the numerical aperture of the focusing lens.

In this work we demonstrate the ability of the PA tomography device to create 3D images with constant resolution throughout the volume enclosed by the scanning optical beam.

Furthermore, two scanning modes of the beam around an object are compared, and finally the imaging of a complex biological sample (an isolated mouse heart) is demonstrated.

## **2. PA tomography with line detectors**

The principles of signal acquisition and image reconstruction have in detail been described elsewhere<sup>12-15</sup>, therefore only a short overview is given here. For an exact reconstruction it is necessary to scan the entire acoustic field around the object with the line detector. The line always moves in a way that it is perpendicular to one single axis, about which the object is rotated. For one rotational angle, the scanning path of the detector should preferentially be a closed curve in the plane perpendicular to the line direction, completely surrounding the object. From a set of such measurements it is possible to reconstruct a 2D projection of the initial distribution of pressure in the object,  $p^{2D}(u, v, t = 0)$ , generated by a short laser pulse. Here, the variables  $u$  and  $v$  are coordinates perpendicular to the line direction in the frame rotated relative to the object. The rotation axis is parallel to the  $v$ -direction. Due to the integration of the acoustic field along the line, this reconstruction problem is strictly two-dimensional. When projections over a total angle of  $\pi$  rad are acquired, the next step in 3D image reconstruction is the application of the inverse Radon transform to all planes perpendicular to the rotation axis. Since the inverse Radon transform is a standard mathematical operation usually implemented in software such as Matlab, our previous studies have focused mainly on the 2D reconstruction problem. A single linear scan combined with a

frequency domain reconstruction was proposed first<sup>12</sup>. Later, we worked on refinements with other scan geometries like a half circle, an L-shaped or even arbitrarily shaped curve using time-domain back projection, frequency-domain or time reversal reconstruction<sup>14-16</sup>. We also addressed the problem of limited view data acquisition and found special weight functions that can be included in a back projection algorithm to reduce the level of artifacts in the case that the complete object is in a region where the detection aperture is between  $\pi$  and  $2\pi$  rad, where  $\pi$  is the minimum required aperture for exact reconstruction in 2D<sup>14,17</sup>.

In the present study, two scan geometries are employed, which have turned out to be well suited for 3D imaging. Both are open curves, providing access for holding and manipulating the sample. The first one uses a combination of three linear scans, forming an open box that encloses the object from three sides (Fig. 2). The advantage of using linear scans is the possibility to use a fast, frequency-domain (FD) reconstruction algorithm. It was first introduced for 3D imaging, where a point detector scans a plane next to the object<sup>18,19</sup> and can easily be adapted to 2D imaging, where the detector scans along a straight line<sup>14,20</sup>. Because a finite scan length introduces strong artifacts due to missing data for points lying about  $\frac{1}{2}$  scan length above the detection line, the idea is to acquire data along at least a second detection line perpendicular to the first one and also to add the resulting images, either in frequency or in real space<sup>14,21</sup>. The third line scan is added to provide a detection aperture of at least  $\pi$  rad for all points localized inside the open box. A problem here is the varying detection aperture within the imaging volume. We follow the suggestion made by Xu et al.<sup>10</sup> to weight the reconstructed image with  $2\pi/\Psi(u, v)$ , where  $\Psi(u, v)$  is the spatially varying detection aperture angle.

The second imaging geometry is a half circular scan of the line detector around the sample (Fig. 2). Although for such a  $\pi$ -arc scanning curve also a FD reconstruction is possible using an algorithm for a closed circular scan<sup>14,22</sup> with missing data, we prefer here the 2D version of a filtered back projection algorithm<sup>15,17</sup>. It was originally developed for 3D imaging with

point detectors where it was found to give accurate reconstructions for detection surfaces in the shape of a closed sphere, a closed cylinder or an infinite plane<sup>23</sup>. The advantage of this imaging procedure is that in the back projection for each reconstruction – detection point pair an individual weight factor can be applied, which can be used to improve the image quality in limited view imaging, providing more accurate relative amplitude values and reducing the “duplicate direction” artifact<sup>17</sup>. The applied weight factors reduce the contribution of detectors, which lie on opposite points on the detection curve with respect to a reconstructed point in a way that they complement each other to one. Detectors having no opposite point on the detection curve receive a weight equal to one. Such individual weight factors are not possible for the FD reconstruction. However, in order to achieve a similar effect for points lying near the center of the box, the reconstructions from the two line scans on the sides of the box are weighted with 0.5, whereas the line scan at the bottom of the box receives a weight of 1.

The line detector used in this study is a light beam propagating in water. Its advantage over a detector formed by a strip of piezoelectric polymer film is its omni directional sensitivity in the plane perpendicular to the line<sup>24</sup>. Imaging with such a line detector should give a 3D image with constant resolution throughout an imaging volume that is limited by the detection surface (i.e. the surface touched by the scanning line while the sample is rotated)<sup>25</sup>. The resolution should be limited by the temporal resolution of the line detector, which is mainly due to its finite diameter. This is valid under the assumption that the angular step size for rotating the sample obeys the rules known from tomographic imaging, essentially requiring that the number of spatial samples along one projection (in  $u$ -direction of the 2D reconstruction) should be approximately equal to the number of projection angles<sup>26</sup>.

### 3. Simulations

Simulations were performed to compare the two scanning geometries on an identical phantom and to investigate the variation of 3D image quality within the imaging volume. A phantom was therefore constructed that in one plane filled the entire imaging volume as completely as possible. The phantom consisted of uniformly heated spheres, for which an analytical photoacoustic signal can be calculated<sup>15</sup>. The simulations were performed assuming constant speed of sound and excluding acoustic attenuation. The 2D projection images were reconstructed on a grid of 200 x 200 points. For the  $\pi$ -arc scan, the number of signals along the arc was 200. For the box-scan, the number of detection points on each side had to be 200, because the spatial increment of the measurement automatically becomes the increment of the reconstructed image. Finally, in both cases 200 projections were calculated while rotating the phantom 180°.

Figure 3 shows the cross section of the original phantom in part (a). The corresponding sections of the reconstructed 3D image are shown in (b) for the  $\pi$ -arc and filtered back projection and in (c) for the box scan using FD reconstruction. Part (d) and (e) compare horizontal and vertical profiles, respectively, through the center of the phantom.

Both reconstructions show sharp edges of the spheres, even at the periphery of the reconstruction volume. The exactness of the back projection reconstruction is generally slightly higher, as indicated by the more accurate amplitude values, the better uniformity of amplitudes over the imaging volume and by the absence of artifacts as they appear in the FD reconstruction mainly along the vertical direction. Also a slight distortion of the spheres is seen in the FD reconstruction near the detection curve. The FD algorithm, on the other hand, is considerably faster than the filtered back projection with weighting. In the simulations, the reconstruction of the 200 x 200 points area of one projection took 6.7 s with the back projection algorithm and 1.0 s with the FD algorithm. Taking into account that the latter used three times more detector points, the back projection turns out to be slower by a factor of 20.

## 4. Experiment

### 4.1 Imaging device

As an approximate line sensor we used a light beam from a continuous laser, in a Mach-Zehnder interferometer configuration (Fig. 4)<sup>12</sup>. The temporal resolution of this detector is limited by the beam diameter of about 40  $\mu\text{m}$  in the waist of the focused beam. The imaging range, which is the range along the line detector where this high resolution can be achieved, is given by the focal depth of 16 mm<sup>24</sup>. These are the measured values for the used focal length and numerical aperture. Higher resolution would require tighter focusing at the expense of a smaller imaging range.

For scanning, the sample was moved relative to the laser beam using two computer controlled linear stages. Additionally, the sample was mounted on a rotation stage. At each position of the line detector relative to the object only a single signal was acquired, without averaging. Samples were illuminated by pulses from an optical parametric oscillator (OPO) with a pulse duration between 5 and 8 ns.

### 4.2 Samples

A phantom consisting of black human hairs (photograph in the inset of Fig. 5(a)) was used to demonstrate the constant resolution. It was imaged using the  $\pi$ -arc scan with 91 detector positions along an arc with a radius of 10 mm and 200 angular positions of the arc relative to the sample, spanning a range of 180°. The acoustic waves were excited by illuminating the hair phantom with laser pulses at a wavelength of 502 nm from two directions as shown in Fig. 4. Limited by the 10 Hz pulse repetition rate of the laser the data acquisition for the 3D image took about 30 min.

The second object was an isolated mouse heart prepared as follows. Immediately after excision the still beating heart of an anesthetized mouse was placed in a 4% formaldehyde solution for fixation. Since the heart continues beating for a short time after removal the

remaining blood is flushed out and replaced by the formaldehyde solution. For PA imaging the heart was finally embedded into agarose to improve acoustic coupling. Illuminated with pulses in the near infrared range at a wavelength of 750 nm also inner structures of the mouse heart were visualized because of the increased penetration of the light at this wavelength. The pulses with a fluence of 12 mJ/cm<sup>2</sup> illuminated one side of the object from a direction parallel to the detection laser beam. The mouse heart was rotated to 179 angular positions over a range of 360°. At each rotational position, the detector scanned a box formed by three linear scans of 18 mm length and an increment of 72 μm, giving 750 detector positions in total. Using those scanning parameters the data acquisition took about four hours.

## **5. Results**

### *5.1. Hair phantom*

Reconstructed images of the hair phantom are shown in Fig. 5 as maximum amplitude projections in three orthogonal directions. The inset in figure part (a) shows the photograph of the phantom. The width of the hair that was located in the center of the phantom is drawn in Fig. 5(d) as a function of position along the hair. This diagram shows the dependence of width in vertical and in horizontal directions, taken from projections in (a) and (b), respectively. The widths stay constant over the length of the hair and are slightly different for horizontal and vertical direction. Considering the thickness of the hair (60 μm) the measured width is consistent with the expected resolution of about 40 μm, given by the laser beam diameter in the focal region.

### *5.2. Mouse heart*

Figure 6 shows 4 sections through the 3D image of the mouse heart. Sections in (b), (c) and (d) are perpendicular to the section (a), where the positions of the three other sections are indicated as black arrows. In order to see the relatively faint structures formed by the heart

muscle tissue together with the more strongly absorbing structures probably caused by absorption in blood remnants, we chose to display the square root of the reconstructed relative energy density. The inner structures of the heart, such as the left and right ventricles, the left atrium and the papillary muscles can be clearly distinguished. Also the very fine structure of a mitral valve can be seen in two sections.

## 6. Discussion

Photoacoustic micro-tomography for biological or pre-clinical research is mainly designed for imaging of excised biological samples or of anesthetized small animals. Other than in photoacoustic *in vivo* imaging, speed has not such a high priority as accuracy and resolution. It is therefore feasible to use a single scanning detector for acquisition of photoacoustic signals. The proposed focused laser beam detector requires the sample to be submerged in a coupling liquid but no contact of a physical transducer with the sample. In this kind of “non-contact” detection mode the position of the sensor relative to the sample can be controlled with great accuracy, as it is required for resolving structures with micrometer precision. A drawback is that the high resolution, below 100  $\mu\text{m}$ , can only be achieved in the focal range of the sensor beam. The sample must therefore be carefully positioned next to the focus. For larger samples, where this is not possible, an alternative is the use of a guided laser beam, either in an optical fiber or in a planar waveguide<sup>27-29</sup>.

Comparing the image quality, back projection reconstruction of  $\pi$ -arc data turned out to give better results, partly due to the employed weight factors that give a more accurate reconstruction in case of limited view imaging. The FD reconstruction using box scan data was considerably faster and therefore allows for an easier handling of larger amounts of data. This is an advantage in case of more complex samples, where small scan increments and therefore a large number of detection points are essential. The box-scan was therefore chosen for imaging of the mouse heart.

The dataset of the mouse heart shown in Fig. 6 was recorded for a currently ongoing study of a cardiac infarct model. In this study several artificially infarcted mouse hearts are investigated using different imaging modalities (photoacoustic, micro CT, histology, MRI). This study is performed to compare the different image representations of infarcted tissue and to determine whether the different imaging modalities can provide complementary information. Furthermore, photoacoustic measurements of the same heart are performed at different wavelengths to evaluate the possibility of an accurate discrimination of different tissues by their absorption spectra. The results of this study will be presented in forthcoming publications.

At this time using a single line detector the imaging time is in the range of hours. It is mainly determined by the repetition rate of the laser and by the amount of detection points along the scanning curve. An obvious improvement, providing a reduction of data acquisition time by a factor of about 100 is therefore the use of a pulsed laser with a repetition rate in the kilohertz range. Another approach, which we currently pursue is to speed up the data acquisition by using some kind of parallel detection to avoid the time consuming scanning around the object. In conclusion, photoacoustic tomography with a scanning, free laser beam and interferometric detection can provide 3D images with a spatially constant resolution in the range of tens of micrometers and has been shown to provide images revealing fine anatomic structures in an excised biological sample.

#### *Acknowledgments*

This work is supported by the Austrian Science Fund, project numbers S 10502-N20, S 10503-N20, S10504-N20 and S10505-N2

## References

1. J. C. Elliott and S. D. Dover, "X-Ray Microtomography," *Journal of Microscopy-Oxford* **126**, 211-213 (1982).
2. R. A. Kruger, W. L. Kiser, D. R. Reinecke, and G. A. Kruger, "Thermoacoustic Computed Tomography Using a Conventional Linear Transducer Array," *Medical Physics* **30**, 856-860 (2003).
3. S. A. Ermilov, T. Khamapirad, A. Conjusteau, M. H. Leonard, R. Lacewell, K. Mehta, T. Miller, and A. A. Oraevsky, "Laser Optoacoustic Imaging System for Detection of Breast Cancer," *Journal of Biomedical Optics* **14**, (2009).
4. M. H. Xu and L. V. Wang, "Photoacoustic Imaging in Biomedicine," *Review of Scientific Instruments* **77**, 041101 (2006).
5. B. T. Cox, S. R. Arridge, K. P. Kostli, and P. C. Beard, "Two-Dimensional Quantitative Photoacoustic Image Reconstruction of Absorption Distributions in Scattering Media by Use of a Simple Iterative Method," *Applied Optics* **45**, 1866-1875 (2006).
6. J. Laufer, D. Delpy, C. Elwell, and P. Beard, "Quantitative Spatially Resolved Measurement of Tissue Chromophore Concentrations Using Photoacoustic Spectroscopy: Application to the Measurement of Blood Oxygenation and Haemoglobin Concentration," *Physics in Medicine and Biology* **52**, 141-168 (2007).
7. X. D. Wang, X. Y. Xie, G. N. Ku, and L. V. Wang, "Noninvasive Imaging of Hemoglobin Concentration and Oxygenation in the Rat Brain Using High-Resolution Photoacoustic Tomography," *Journal of Biomedical Optics* **11**, (2006).
8. H. F. Zhang, K. Maslov, G. Stoica, and L. V. Wang, "Functional Photoacoustic

- Microscopy for High-Resolution and Noninvasive in Vivo Imaging," *Nature Biotechnology* **24**, 848-851 (2006).
9. E. Z. Zhang, J. G. Laufer, R. B. Pedley, and P. C. Beard, "In vivo high-resolution 3D photoacoustic imaging of superficial vascular anatomy," *Phys. Med. Biol.* **54**, 1035-1046 (2009).
  10. Y. Xu, L. V. Wang, G. Ambartsoumian, and P. Kuchment, "Reconstructions in limited-view thermoacoustic tomography," *Medical Physics* **31**, 724-733 (2004).
  11. M. H. Xu and L. V. Wang, "Analytic explanation of spatial resolution related to bandwidth and detector aperture size in thermoacoustic or photoacoustic reconstruction," *Physical Review E* **67**, 056605 (2003).
  12. G. Paltauf, R. Nuster, M. Haltmeier, and P. Burgholzer, "Photoacoustic tomography using a Mach-Zehnder interferometer as acoustic line detector," *Appl. Opt.* **46**, 3352-3358 (2007).
  13. P. Burgholzer, C. Hofer, G. Paltauf, M. Haltmeier, and O. Scherzer, "Thermoacoustic tomography with integrating area and line detectors," *IEEE Trans. Ultrason., Ferroelect., Freq. Contr.* **52**, 1577-1583 (2005).
  14. G. Paltauf, R. Nuster, M. Haltmeier, and P. Burgholzer, "Experimental evaluation of reconstruction algorithms for limited view photoacoustic tomography with line detectors," *Inverse Problems* **23**, S81-S94 (2007).
  15. P. Burgholzer, J. Bauer-Marschallinger, H. Grun, M. Haltmeier, and G. Paltauf, "Temporal Back-Projection Algorithms for Photoacoustic Tomography With Integrating Line Detectors," *Inverse Problems* **23**, 65-80 (2007).

16. P. Burgholzer, G. Matt, M Haltmeier, and G. Paltauf, "Exact and approximative imaging methods for photoacoustic tomography using an arbitrary detection surface," *Phys. Rev. E* **75**, 046706 (2007).
17. G. Paltauf, R. Nuster, and P. Burgholzer, "Weight factors for limited angle photoacoustic tomography," *Phys. Med. Biol.* **54**, 3303-3314 (2009).
18. K. P. Kostli, M. Frenz, H. Bebie, and H. P. Weber, "Temporal Backward Projection of Optoacoustic Pressure Transients Using Fourier Transform Methods," *Physics in Medicine and Biology* **46**, 1863-1872 (2001).
19. Y. Xu, D. Z. Feng, and L. V. Wang, "Exact Frequency-Domain Reconstruction for Thermoacoustic Tomography - I: Planar Geometry," *IEEE Transactions on Medical Imaging* **21**, 823-828 (2002).
20. K. P. Köstli and P. C. Beard, "Two-Dimensional Photoacoustic Imaging by Use of Fourier- Transform Image Reconstruction and a Detector With an Anisotropic Response," *Appl. Opt.* **42**, 1899-1908 (2003).
21. G. Paltauf, R. Nuster, P. Burgholzer, and M Haltmeier "Three-dimensional photoacoustic tomography using acoustic line detectors," *Proc. SPIE* **6437**, 64370N (2007).
22. M. Haltmeier, O. Scherzer, P. Burgholzer, R. Nuster, and G. Paltauf, "Thermoacoustic tomography & the circular Radon transform: Exact inversion formula," *Mathematical Models and Methods in Applied Sciences* **17**, 635-655 (2007).
23. M. H. Xu and L. V. Wang, "Universal back-projection algorithm for photoacoustic computed tomography," *Phys. Rev. E* **71**, 016706 (2005).
24. G. Paltauf, R. Nuster, and P. Burgholzer, "Characterization of integrating ultrasound

- detectors for photoacoustic tomography," *J. Appl. Phys.* **105**, 102026 (2009).
25. M. Haltmeier, O. Scherzer, and G. Zangerl "Influence of Detector Bandwidth and Detector Size to the Resolution of Photoacoustic Tomography," *Proc. ARGESIM-Report* **35**, (2009).
26. A. C. Kak and M. Slaney, *Principles of Computerized Tomographic Imaging* (IEEE Press, New York 1988).
27. H. Gruen, G. Paltauf, M. Haltmeier, and P. Burgholzer "Photoacoustic tomography using a fiber based Fabry-Perot interferometer as an integrating line detector and image reconstruction by model-based time reversal method," *Proc. SPIE* **6631**, 663107 (2007).
28. H. Grün, T. Berer, P. Burgholzer, R. Nuster, and G. Paltauf, "Three Dimensional Photoacoustic Imaging Using Fiber-Based Line Detectors," *Journal of Biomedical Optics* (2010).
29. R. Nuster, G. Paltauf, H. Ditlbacher, and P. Burgholzer "Development of waveguide sensors for the application in photoacoustic tomography," *Proc. SPIE* **6631**, 6631-06 (2007).

List of figure captions:

Fig. 1 Schematic drawing of the focused free propagating laser beam acting as integrating acoustic wave detector.

Fig. 2 Comparison of the  $\pi$ -arc and box scanning curves that are used for 3D-imaging.

Fig. 3 Simulation of 3D imaging with the line detector. (a) Cross section of the original phantom consisting of spheres distributed in the imaging area; (b) and (c) show results of the reconstructed cross section images using the filtered back projection algorithm for the  $\pi$ -arc scanning mode (b) and the FD algorithm for the box scanning mode(c). (d) and (e) compare horizontal and vertical profiles, respectively, through the center of the images (a)-(c). The profiles are taken from the images of the original phantom (dashed line), of the reconstruction using FD algorithm (thick solid line) and of the reconstruction using the filtered back projection algorithm (thin solid line).

Fig. 4 Mach-Zehnder interferometer as an acoustic line detector. BS: beam splitter, L: lens, M: mirror, M+PT: piezo-actuator with mounted mirror, BPD: balanced photo detector (bandwidth 80MHz), BPF: optical band-pass filter, HPF: electronic high-pass filter

Fig. 5 The maximum amplitude projections in three orthogonal directions, (a)-(c), of the reconstructed image of the human hair phantom. Inset of (a) shows a photograph of the phantom. The width of the hair that was located in the center of the phantom is drawn in (d) as a function of position along the hair in vertical (thick solid line) and in horizontal direction (dashed line).

Fig. 6 Four sections of the 3D-image of a mouse heart. (b)-(c) are sections oriented perpendicular to section (a) labeled with black arrows from top to bottom. RV, LV: right and left ventricle; CV: mitral valve; LA: left atrium; PM: papillary muscles

Figures:

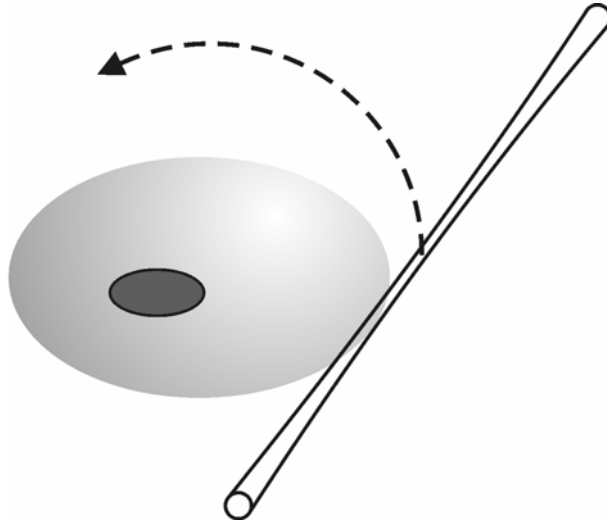


Fig. 1 Schematic drawing of the focused free propagating laser beam acting as integrating acoustic wave detector.

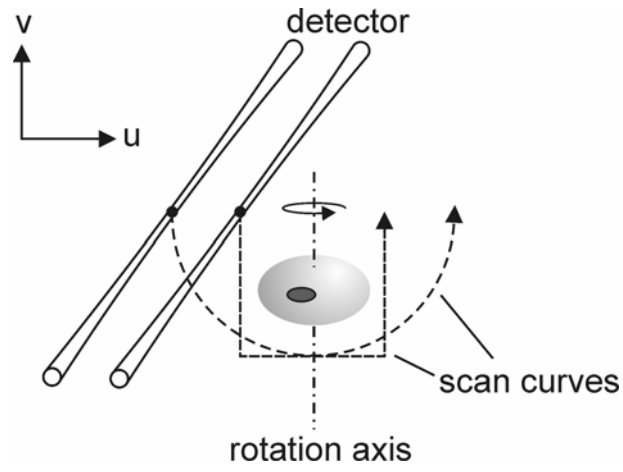


Fig. 2 Comparison of the  $\pi$ -arc and box scanning curves that are used for 3D-imaging.

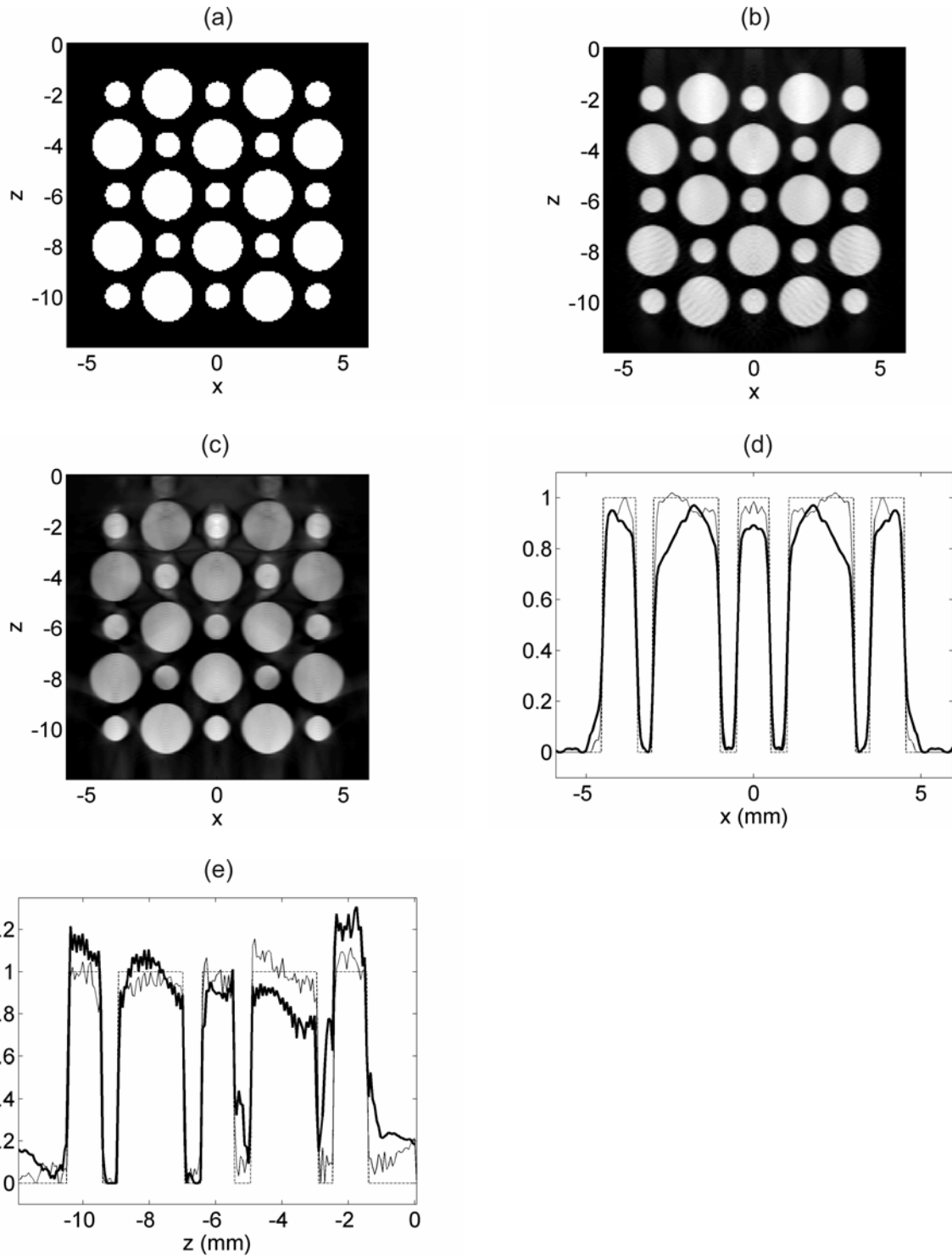


Fig. 3 Simulation of 3D imaging with the line detector. (a) Cross section of the original phantom consisting of spheres distributed in the imaging area; (b) and (c) show results of the reconstructed cross section images using the filtered back projection algorithm for the  $\pi$ -arc scanning mode (b) and the FD algorithm for the box scanning mode (c). (d) and (e) compare horizontal and vertical profiles, respectively, through the center of the images (a)-(c). The profiles are taken from the images of the original phantom (dashed line), of the

reconstruction using FD algorithm (thick solid line) and of the reconstruction using the filtered back projection algorithm (thin solid line).

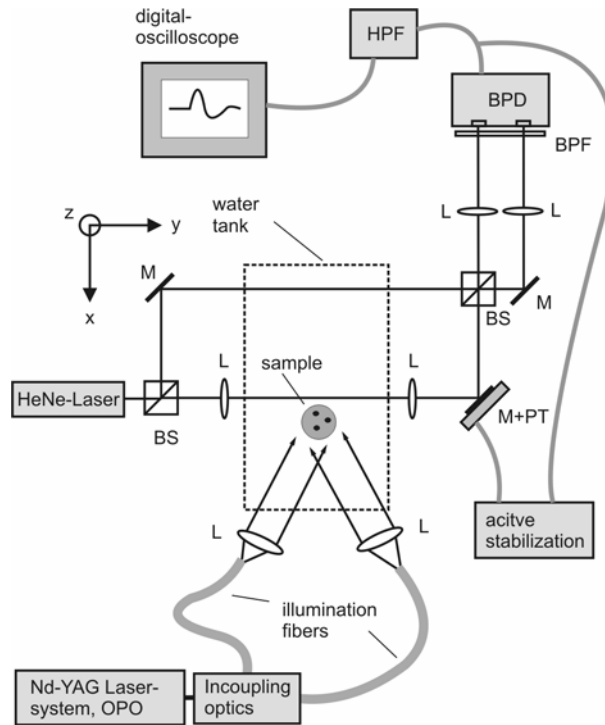


Fig. 4 Mach-Zehnder interferometer as an acoustic line detector. BS: beam splitter, L: lens, M: mirror, M+PT: piezo-actuator with mounted mirror, BPD: balanced photo detector (bandwidth 80MHz) , BPF: optical band-pass filter, HPF: electronic high-pass filter

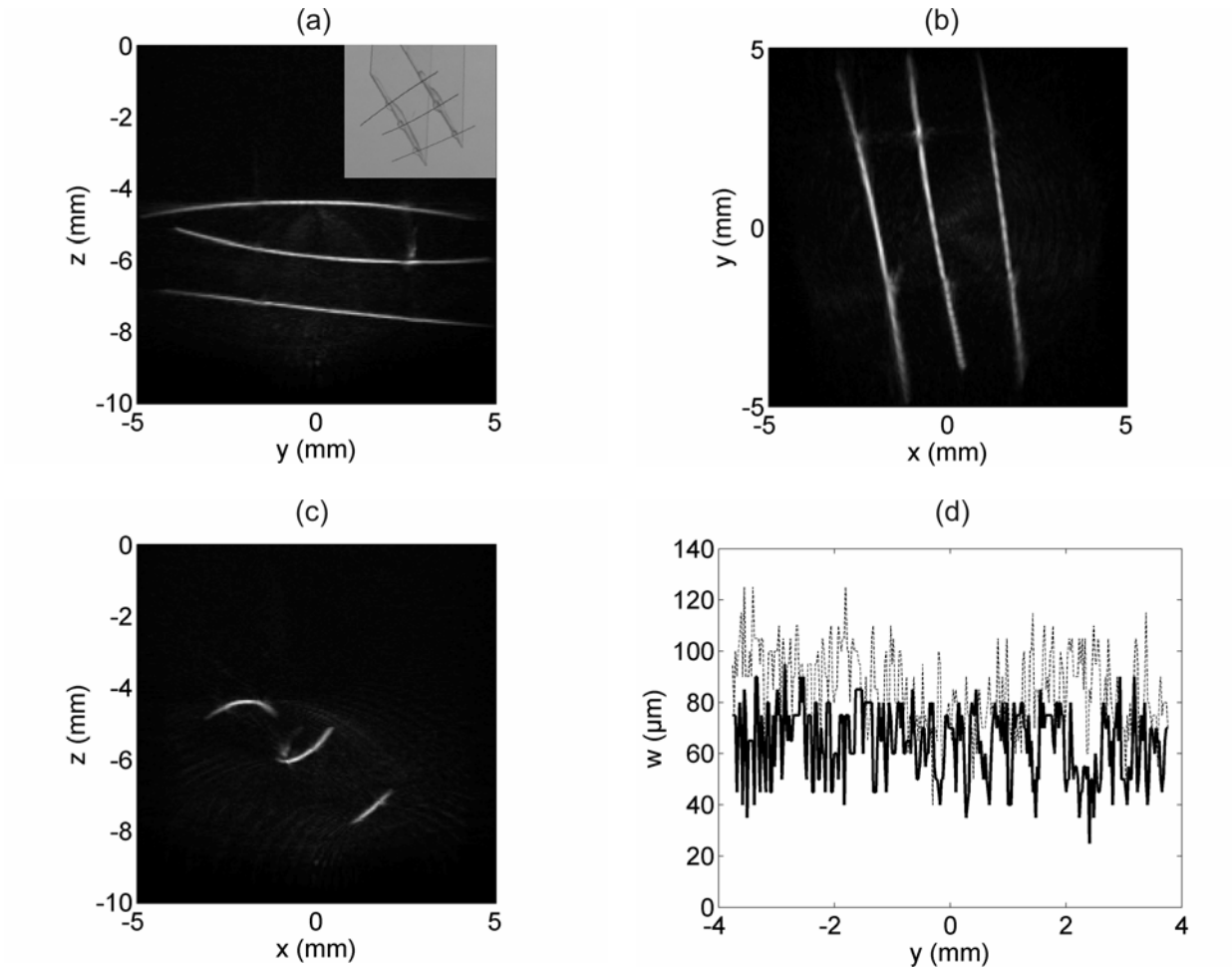


Fig. 5 The maximum amplitude projections in three orthogonal directions, (a)-(c), of the reconstructed image of the human hair phantom. Inset of (a) shows a photograph of the human hair phantom. The width of the hair that was located in the center of the phantom is drawn in (d) as a function of position along the hair in vertical (thick solid line) and in horizontal direction (dashed line).

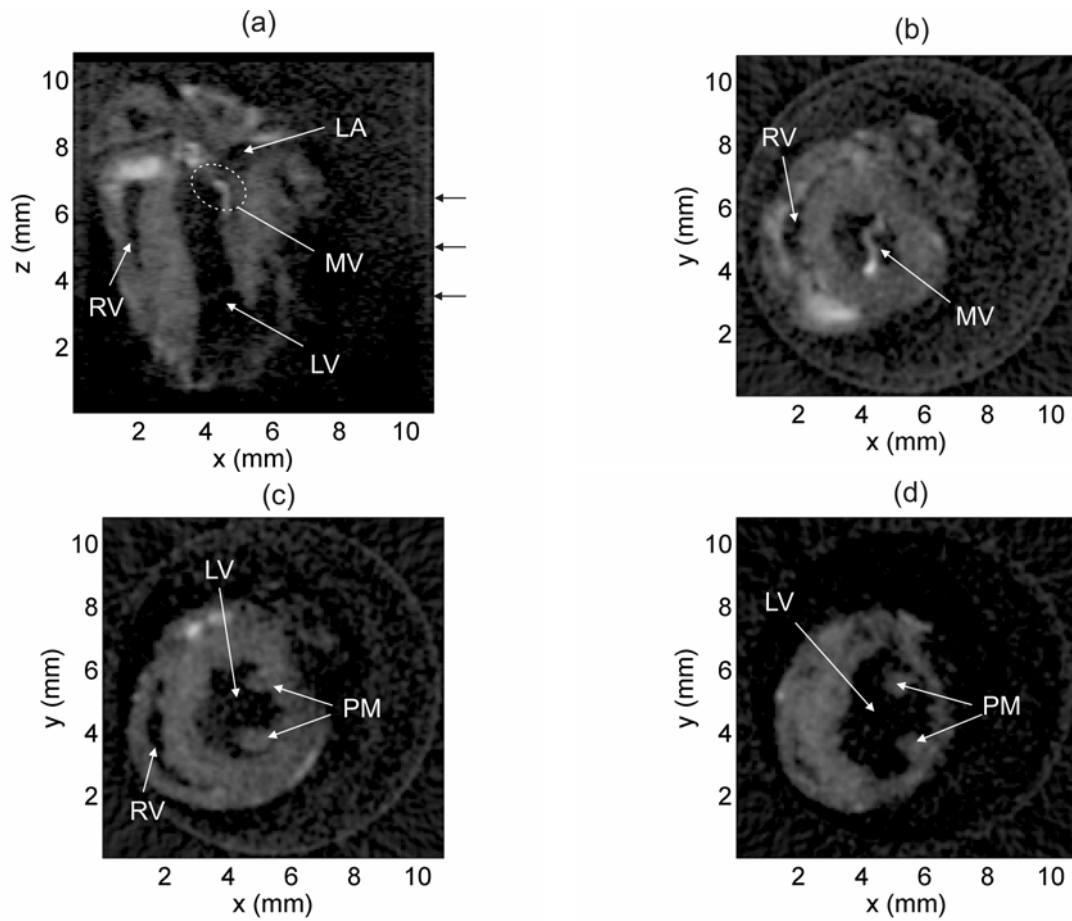


Fig. 6 Four sections of the 3D-image of a mouse heart. (b)-(c) are sections oriented perpendicular to section (a) labeled with black arrows from top to bottom. RV, LV: right and left ventricle; CV: mitral valve; LA: left atrium; PM: papillary muscles